

Estimation of the full-field dynamic response of a floating bridge using Kalman-type filtering algorithms

Petersen, Oyvind W.; Øiseth, Ole; Nord, Torodd S.; Lourens, E.

DOI

[10.1016/j.ymsp.2018.01.022](https://doi.org/10.1016/j.ymsp.2018.01.022)

Publication date

2018

Document Version

Accepted author manuscript

Published in

Mechanical Systems and Signal Processing

Citation (APA)

Petersen, O. W., Øiseth, O., Nord, T. S., & Lourens, E. (2018). Estimation of the full-field dynamic response of a floating bridge using Kalman-type filtering algorithms. *Mechanical Systems and Signal Processing*, 107, 12-28. <https://doi.org/10.1016/j.ymsp.2018.01.022>

Important note

To cite this publication, please use the final published version (if applicable). Please check the document version above.

Copyright

Other than for strictly personal use, it is not permitted to download, forward or distribute the text or part of it, without the consent of the author(s) and/or copyright holder(s), unless the work is under an open content license such as Creative Commons.

Takedown policy

Please contact us and provide details if you believe this document breaches copyrights. We will remove access to the work immediately and investigate your claim.

Estimation of the full-field dynamic response of a floating bridge using Kalman-type filtering algorithms

Ø.W. Petersen^{a,*}, O. Øiseth^a, T. Nord^a, E. Lourens^b

^aNTNU, Norwegian University of Science and Technology, NO-7491 Trondheim, Norway

^bDelft University of Technology, 2628 CN Delft, The Netherlands

Abstract

Numerical predictions of the dynamic response of complex structures are often uncertain due to uncertainties inherited from the assumed load effects. Inverse methods can estimate the true dynamic response of a structure through system inversion, combining measured acceleration data with a system model. This article presents a case study of the full-field dynamic response estimation of a long-span floating bridge: the Bergøysund Bridge in Norway. This bridge is instrumented with a network of 14 triaxial accelerometers. The system model consists of 27 vibration modes with natural frequencies below 2 Hz, which is solved using a tuned finite element model that takes the fluid-structure interaction with the surrounding water into account. Two methods, a joint input-state estimation algorithm and a dual Kalman filter, are applied to estimate the full-field response of the bridge. The results demonstrate that the displacements and the accelerations can be estimated at unmeasured locations with reasonable accuracy when the wave loads are the dominant source of excitation.

Keywords: structural monitoring; floating bridge; response estimation; Kalman filter

1. Introduction

In many civil engineering structures, the dynamic response is an important variable for determining sufficient structural safety and design. In the design phase, the dynamic response is traditionally obtained using a numerical model of the structure and combinations of load states as dictated by design codes. However, there are uncertainties associated with the load effects and with the how the structure responds to the loads. Consequently, the numerically predicted response has inherited uncertainties, meaning that the design limit states, such as structural failure, instability, fatigue or serviceability, must also be treated as having uncertainties.

Monitoring systems installed on existing structures enable the structural behaviour to be studied under the true operating conditions. The collected data may be used for long-term statistics, model parameter identification, operational modal analysis (OMA) or structural health monitoring (SHM). A shortcoming of full-scale measurements is that only output data are typically available since inputs are often impractical to measure directly on a large scale. In addition, the dynamic response can only be measured at a limited number of points because of cost limitations and/or due to practical restrictions on sensor locations.

In recent years, researchers have explored techniques for using incomplete measurement data to estimate the response at unmeasured locations in structural or mechanical systems. One example of this approach is modal expansion techniques, which

*Corresponding author

Email addresses: oyvind.w.petersen@ntnu.no (Ø.W. Petersen), ole.oiseth@ntnu.no (O. Øiseth), torodd.nord@ntnu.no (T. Nord), e.lourens@tudelft.nl (E. Lourens)

URL: <https://www.ntnu.edu/kt/research/dynamics> (Ø.W. Petersen)

15 can use strain or stress predictions as an indicator of the local utilization of the structural capacity. Modal expansion algorithms
16 have been shown to perform well on offshore wind turbines [1, 2] and platforms [3, 4], estimating strain histories as a tool for
17 monitoring the fatigue service life. Another class of methods consists of filtering techniques for coupled input and state esti-
18 mation, and these techniques are commonly based on Kalman-type filters. Multiple methods have been proposed in the recent
19 literature [5–15]. Among the popular contributions are the algorithm for joint input-state estimation (JIS) [9]. This methodol-
20 ogy has also been developed further [10] and tested in situ [11]. In the proposed dual Kalman filter (DKF) [12], the inputs and
21 states are estimated from two Kalman filters working in conjunction. Experimental testing and verification of the DKF can be
22 found in [13]. The assumptions and structure of the different Kalman-type filters lead to advantages and disadvantages, which
23 means that the applicability of the different methods can vary from one case study to another. The experimental comparison in
24 [14] focuses on the stability in the real-time application of some filter variants. Practical applications of the techniques include
25 strain prediction for fatigue [16] and studies of ice-structure interaction [17, 18]. Other Kalman filter approaches have been
26 used to estimate the responses of tall buildings due to wind loads using acceleration data [19, 20].

27 Although many full-scale measurement campaigns have been conducted on long-span bridges (see, e.g. [21] for a brief
28 overview), the methodologies for full-field response estimation have seen little exploration on these types of structures. This
29 may be explained by several reasons. First, most of the relevant methodologies have been developed quite recently, and the
30 research field is still in active development. Second, long-span bridges typically exhibit a highly complex dynamic behaviour
31 since many modes contribute to the total response. Finally, (non-linear) fluid-structure interaction phenomena can occur, which
32 may be difficult to implement in a model. The implication of the complex dynamics is that accurate system models and
33 dense sensor networks are required for many of the current prevailing methodologies to be applicable. If a system for full-
34 field response monitoring is successfully implemented, then the reward is robust control over the condition of important civil
35 infrastructure.

36 This article focuses on applying filtering techniques to estimate the full-field dynamic response of very large bridges, making
37 use of measured acceleration data together with a numerical model of the structure. We present a case study of a long-span
38 floating bridge, the Bergsøysund Bridge, and assess how well two of the aforementioned filter algorithms, JIS and DKF, are able
39 to reconstruct the global response. Herein, the methodology is tested in full scale on a structure that is in operation using three
40 recorded data sets with different ambient wave and wind conditions. The presented work is a continuation of previous studies
41 [22]; in the current paper, the studies are extended in the use of the methodology and the results are improved. The remainder
42 of this paper is organized as follows: section 2 presents the Bergsøysund bridge and relevant mathematical formulations for
43 floating bridge dynamics. Section 3 is devoted to the response estimation methodology and system model. In section 4, the
44 dynamic response estimation from several time series are shown and the results are discussed. Conclusions are drawn in section
45 5.

46 **2. Floating bridges**

47 *2.1. The Bergsøysund Bridge*

48 The Bergsøysund Bridge (Fig. 1) is located on the midwestern Norwegian coast as a part of the E39 Coastal Highway
49 Route. This bridge opened in 1992 and is a unique type of structure since it is one of a few long-span floating bridges with
50 end support only. The bridge consists of a trusswork of steel tubes and is supported by seven pontoons. The pontoons are shell



Figure 1: Left: The Bergsøysund Bridge viewed from the north end; right: the truss structure as viewed from below the bridge deck. Photo: K.A. Kvåle.

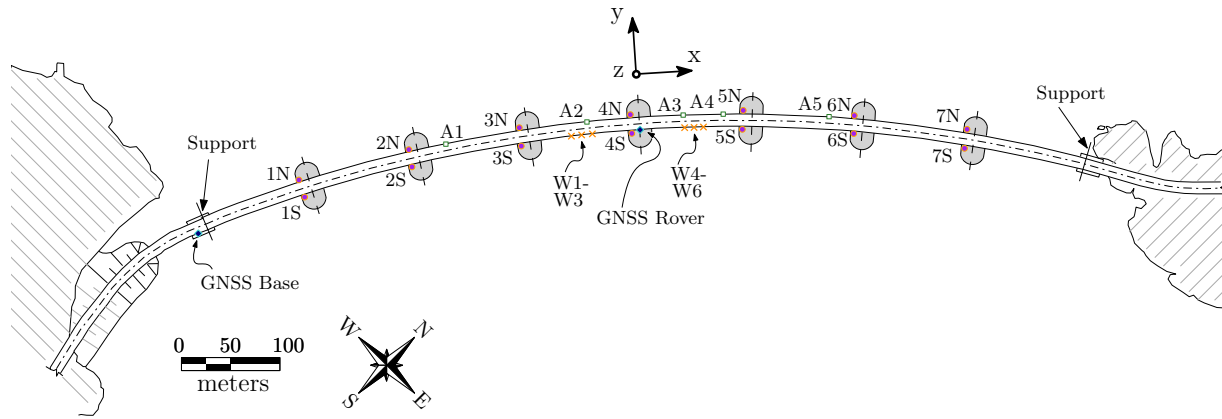


Figure 2: Overhead view of the Bergsøysund Bridge and the locations of the accelerometers (1S-7S, 1N-7N), wave height sensors (W1-W6), anemometers (A1-A5) and GNSS. The axes of the global coordinate system coincide with the major axes of the middle pontoon, which lies on the symmetry line of the bridge.

51 structures that are made from lightweight aggregate concrete. The floating span of the bridge is 840 m long, with free spans of
 52 105 m between the pontoons. Since the bridge has no anchoring, it is susceptible to dynamic excitation, particularly from wave
 53 actions. The construction of similar but longer bridges is planned in the upgrade of the E39 Coastal Highway Route, making
 54 the Bergsøysund Bridge a highly relevant case study for the implementation of monitoring systems on modern infrastructure.

55 The bridge is instrumented with an extensive monitoring system, as shown in Fig. 2. Two triaxial accelerometers are located
 56 at each of the seven pontoons (Fig. 3). The Global Navigation Satellite System (GNSS) station consists of a stationary base
 57 unit at the bridge abutment and a rover unit located at the middle of the bridge (Fig. 3), tracking the displacements using RTK
 58 (Real Time Kinematic) technology. In addition to the vibration data, six wave height sensors and five anemometers collect data
 59 on the ambient conditions at the site. The system continuously monitors the structure, and data are automatically saved when
 60 the wind velocity exceeds a trigger value. For more information, we refer to the paper that describes the monitoring system in
 61 detail [23].



Figure 3: Left: accelerometer mounted on the truss; right: GNSS rover station at the middle of the bridge.

2.2. System equations for a floating bridge

A floating bridge is a system where the structural vibrations are coupled with the fluid motion at the wetted part of the body. Consider a system discretized with n_{DOF} degrees of freedom (DOFs). The governing equations of motion are first formulated in the frequency domain for convenience:

$$-\omega^2 \mathbf{M}(\omega) \mathbf{u}(\omega) + i\omega \mathbf{C}(\omega) \mathbf{u}(\omega) + \mathbf{K}(\omega) \mathbf{u}(\omega) = \mathbf{S}_p \mathbf{p}_w(\omega) \quad (1)$$

where the displacement vector $\mathbf{u}(\omega)$ and the wave excitation forces $\mathbf{p}_w(\omega)$ are Fourier transforms of their time-domain equivalents $\mathbf{u}(t) \in \mathbb{R}^{n_{\text{DOF}}}$ and $\mathbf{p}_w(t) \in \mathbb{R}^{n_p}$, respectively. The selection matrix $\mathbf{S}_p \in \mathbb{R}^{n_{\text{DOF}} \times n_p}$ assigns the wave forces to the DOF that has direct fluid contact. It is assumed that waves are the dominant source of excitation for the bridge. In the structural monitoring assessment by Kvåle and Øiseth [23], it was shown that the dynamic response of the Bergsøysund Bridge is largely dictated by the waves, whereas the direct load effects of the wind for most cases are small in the frequency range of the wave spectrum. The aforementioned study also found that the response to traffic is small compared to waves and is largely high-frequent (>2 Hz).

The system matrices in Eq. 1 can be split into two parts according to their nature of origin:

$$\mathbf{M}(\omega) = \mathbf{M}_s + \mathbf{M}_h(\omega) \quad (2)$$

$$\mathbf{C}(\omega) = \mathbf{C}_s + \mathbf{C}_h(\omega) \quad (3)$$

$$\mathbf{K} = \mathbf{K}_s + \mathbf{K}_h \quad (4)$$

The subscript s denotes that the mass, damping and stiffness matrices \mathbf{M}_s , \mathbf{C}_s and \mathbf{K}_s are related to the structure. Due to the fluid-structure interaction, the hydrodynamic mass $\mathbf{M}_h(\omega)$ and damping $\mathbf{C}_h(\omega)$ are functions of frequency. \mathbf{K}_h is the hydrostatic restoring stiffness, which is assumed to not vary with frequency. When applying the inverse Fourier transform and rearranging terms, Eq. 1 can be written as follows:

$$(\mathbf{M}_s + \mathbf{M}_{h0}) \ddot{\mathbf{u}}(t) + \mathbf{C}_s \dot{\mathbf{u}}(t) + (\mathbf{K}_s + \mathbf{K}_h) \mathbf{u}(t) = \mathbf{S}_p \mathbf{p}_w(t) + \mathbf{S}_p \mathbf{p}_{mi}(t) = \mathbf{S}_p \mathbf{p}(t) \quad (5)$$

78 where $\mathbf{M}_{h0} = \mathbf{M}_h(\omega = 0)$. The term $\mathbf{S}_p \mathbf{p}_{mi}(t)$ are considered as the motion-induced forces here. Using the convolution
79 theorem, the following definition is obtained:

$$\mathbf{S}_p \mathbf{p}_{mi}(t) = -\mathcal{F}^{-1} \left[(i\omega(\mathbf{M}_h(\omega) - \mathbf{M}_{h0}) + \mathbf{C}_h(\omega)) \mathbf{u}(\omega) i\omega \right] = \int_{-\infty}^{\infty} \tilde{\mathbf{k}}(\tau) \dot{\mathbf{u}}(t - \tau) d\tau \quad (6)$$

80 The kernel $\tilde{\mathbf{k}}$ can be viewed as a memory-type function and is defined as follows:

$$\tilde{\mathbf{k}}(t) = \frac{1}{2\pi} \int_{-\infty}^{\infty} (i\omega(\mathbf{M}_h(\omega) - \mathbf{M}_{h0}) + \mathbf{C}_h(\omega)) e^{i\omega t} d\omega \quad (7)$$

81 A choice is made to establish a time-invariant linear system model, which is required for using the algorithms presented
82 in Section 3.1. The formulation in Eq. 5 is interpreted as follows: the terms on the left-hand side constitute a linear system,
83 whereas those on the right-hand side are the input forces applied to the linear system. The wave excitation forces and motion-
84 induced forces, which work in the same set of DOFs, are collected in the hydrodynamic force vector $\mathbf{p}(t) = \mathbf{p}_w(t) + \mathbf{p}_{mi}(t)$. In
85 other words, $\mathbf{p}(t)$ is by definition the input forces as felt by the moving structure.

86 For structures with many DOFs, it is favoured to work with a reduced-order model based on a limited set of vibration modes.
87 A modal reduction of the system in Eq. 5 is performed by solving the following eigenvalue problem:

$$[\mathbf{K}_s + \mathbf{K}_h - \omega_j^2(\mathbf{M}_s + \mathbf{M}_{h0})] \boldsymbol{\phi}_j = \mathbf{0} \quad (j = 1 \dots n_m) \quad (8)$$

88 The mass-normalized "wet" mode shape vectors of the n_m selected modes are collected in the matrix $\boldsymbol{\Phi} \in \mathbb{R}^{n_{DOF} \times n_m}$. Using
89 the relation $\mathbf{u}(t) = \boldsymbol{\Phi} \mathbf{z}(t)$, the modal transform of Eq. 5 reads as follows:

$$\ddot{\mathbf{z}}(t) + \boldsymbol{\Gamma} \dot{\mathbf{z}}(t) + \boldsymbol{\Omega}^2 \mathbf{z}(t) = \boldsymbol{\Phi}^T \mathbf{S}_p \mathbf{p}(t) \quad (9)$$

90 where the structural damping \mathbf{C}_s was assumed proportional. $\boldsymbol{\Gamma} \in \mathbb{R}^{n_m \times n_m}$ and $\boldsymbol{\Omega} \in \mathbb{R}^{n_m \times n_m}$ are both diagonally populated
91 with the natural frequencies ω_j and modal damping ratios ξ_j :

$$\boldsymbol{\Omega} = \text{diag}(\omega_1, \omega_2, \dots, \omega_{n_m}), \quad \boldsymbol{\Gamma} = \text{diag}(2\omega_1 \xi_1, 2\omega_2 \xi_2, \dots, 2\omega_{n_m} \xi_{n_m}) \quad (10)$$

92 We emphasize that the modal properties are inherited from the chosen linear system as defined in Eq. 5. In other words, the
93 modal quantities do not correspond to solving the complex eigenvalue problem of the system in Eq. 1, which can be desired for
94 frequency-domain studies of floating structures (see, e.g. [24]). A discrete-time state-space representation of Eq. 9 is formulated
95 under the assumption of a zero-order hold on the force:

$$\mathbf{x}_{k+1} = \mathbf{A} \mathbf{x}_k + \mathbf{B} \mathbf{p}_k \quad (11)$$

96 where the sample rate is set to $F_s = 1/\Delta t$. \mathbf{x}_k is the modal state vector, and \mathbf{p}_k is the force vector at time instant $t_k = k\Delta t$
97 ($k = 0, 1, \dots, N$):

$$\mathbf{x}_k = \begin{bmatrix} \mathbf{z}(t_k) \\ \dot{\mathbf{z}}(t_k) \end{bmatrix}, \quad \mathbf{p}_k = \mathbf{p}(t_k) \quad (12)$$

98 The state transition matrix $\mathbf{A} \in \mathbb{R}^{2n_m \times 2n_m}$ and input matrix $\mathbf{B} \in \mathbb{R}^{2n_m \times n_p}$ are given as follows:

$$\mathbf{A} = \exp\left(\begin{bmatrix} \mathbf{0} & \mathbf{I} \\ -\mathbf{\Omega}^2 & -\mathbf{\Gamma} \end{bmatrix} \Delta t\right), \quad \mathbf{B} = (\mathbf{A} - \mathbf{I}) \begin{bmatrix} \mathbf{0} & \mathbf{I} \\ -\mathbf{\Omega}^2 & -\mathbf{\Gamma} \end{bmatrix}^{-1} \begin{bmatrix} \mathbf{0} \\ \mathbf{\Phi}^T \mathbf{S}_p \end{bmatrix} \quad (13)$$

99 Next, acceleration and displacement measurements are considered. The output vector $\mathbf{y} \in \mathbb{R}^{n_d}$ reads as follows:

$$\mathbf{y}_k = \mathbf{S}_d \mathbf{u}(t_k) + \mathbf{S}_a \ddot{\mathbf{u}}(t_k) = \mathbf{G} \mathbf{x}_k + \mathbf{J} \mathbf{p}_k \quad (14)$$

100 where the boolean matrices $\mathbf{S}_a \in \mathbb{R}^{n_d \times n_{\text{DOF}}}$ and $\mathbf{S}_d \in \mathbb{R}^{n_d \times n_{\text{DOF}}}$ select the measured DOFs. $\mathbf{G} \in \mathbb{R}^{n_d \times n_m}$ and $\mathbf{J} \in \mathbb{R}^{n_d \times n_p}$ denote
101 the output influence matrix and direct transmission matrix, respectively:

$$\mathbf{G} = \begin{bmatrix} \mathbf{S}_d \mathbf{\Phi} - \mathbf{S}_a \mathbf{\Phi} \mathbf{\Omega}^2 & -\mathbf{S}_a \mathbf{\Phi} \mathbf{\Gamma} \end{bmatrix}, \quad \mathbf{J} = \begin{bmatrix} \mathbf{S}_a \mathbf{\Phi} \mathbf{\Phi}^T \mathbf{S}_p \end{bmatrix} \quad (15)$$

Zero-mean white noise vectors are added to Eq. 11 and 14, which completes the stochastic state-space representation:

$$\mathbf{x}_{k+1} = \mathbf{A} \mathbf{x}_k + \mathbf{B} \mathbf{p}_k + \mathbf{w}_k \quad (16)$$

$$\mathbf{y}_k = \mathbf{G} \mathbf{x}_k + \mathbf{J} \mathbf{p}_k + \mathbf{v}_k \quad (17)$$

102 The following covariance relations describe the process noise \mathbf{w}_k and measurement noise \mathbf{v}_k :

$$\mathbb{E}[\mathbf{w}_k \mathbf{w}_l^T] = \mathbf{Q} \delta_{kl}, \quad \mathbb{E}[\mathbf{v}_k \mathbf{v}_l^T] = \mathbf{R} \delta_{kl}, \quad \mathbb{E}[\mathbf{w}_k \mathbf{v}_l^T] = \mathbf{S} \delta_{kl} \quad (18)$$

103 Finally, an additional equation is introduced for the DKF, in which the force evolution is modelled as a random walk:

$$\mathbf{p}_{k+1} = \mathbf{p}_k + \boldsymbol{\eta}_k \quad (19)$$

104 Additionally, $\boldsymbol{\eta}_k$ is a zero-mean white noise vector. Its prescribed covariance matrix $\mathbb{E}[\boldsymbol{\eta}_k \boldsymbol{\eta}_l^T] = \mathbf{Q}_p \delta_{kl}$ can be viewed as a
105 regularization parameter that controls the force magnitude.

106 3. Application of filtering methodology

107 3.1. Filtering algorithms

108 Modelling of complex systems usually involves significant uncertainties on the state variables in addition to the measure-
109 ment uncertainties. Deterministic-stochastic techniques are therefore in this study chosen over classic deterministic approaches
110 to identification, where typically only measurement noise is considered. Two methods will be used for estimating the response.
111 The first method is the aforementioned joint-input state estimation algorithm (JIS) [9, 10]. The second method is the dual
112 Kalman filter (DKF) [12]. The equations of the filters are given in Appendix A; for a detailed explanation of the algorithms, we
113 refer to the original works [9, 12]. Both methods are based on minimum-variance unbiased estimation of the states and input
114 forces. The resulting uncertainty on the obtained estimates is also provided by the algorithms, provided that the (true) noise
115 statistics (\mathbf{Q} , \mathbf{R} and \mathbf{S}) are known.

116 Some practical differences between the two methods can be mentioned. The DKF is distinguished for its ability to mitigate
117 the instabilities that can occur when only acceleration data is available. This comes at the cost of having to specify an additional

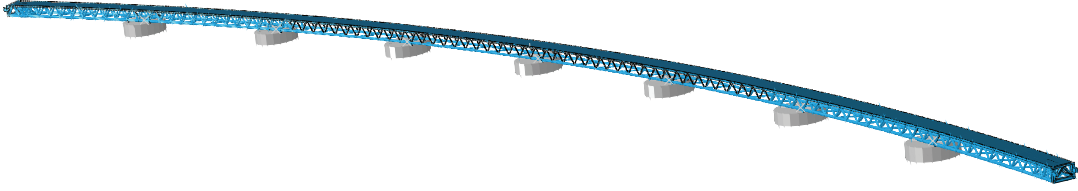


Figure 4: The FE model of the bridge. The displayed pontoons are non-structural elements for visualization purposes only.

118 parameter, namely the covariance matrix \mathbf{Q}_P . The JIS makes no prior assumption on the evolution of the forces, which is an
 119 advantage in the sense that less information on the problem at hand is required prior to filtering. It can however suffer from
 120 instabilities when only acceleration data is available, which can only be removed by also including displacement or strain data.

121 When estimates of the system states ($\hat{\mathbf{x}}$) and forces ($\hat{\mathbf{p}}$) are available from these filtering algorithms, displacements or
 122 accelerations can be estimated in any DOF using Eq. 20 or 21, respectively:

$$\hat{\mathbf{y}}_k = \mathbf{S}'_d \mathbf{u}(t_k) = \mathbf{S}'_d \begin{bmatrix} \Phi & \mathbf{0} \end{bmatrix} \hat{\mathbf{x}}_k \quad (20)$$

$$\hat{\mathbf{y}}_k = \mathbf{S}'_a \ddot{\mathbf{u}}(t_k) = \mathbf{G}' \hat{\mathbf{x}}_k + \mathbf{J}' \hat{\mathbf{p}}_k \quad (21)$$

123 where \mathbf{S}'_d or \mathbf{S}'_a now selects the considered DOFs, and \mathbf{G}' and \mathbf{J}' can be determined using Eq. 15.

124 3.2. System model and sensor network

125 There are two triaxial accelerometers at each of the seven pontoons, which means that 42 acceleration outputs are available.
 126 However, not all the output signals are linearly independent due to the pairwise allocation of the sensors. Seven output signals
 127 (1N Y, 2N Y, 3N Y, 4N Y, 5N Y, 6N Y and 7N Y) are therefore discarded as redundant data (cf. Fig 2). In addition, the two
 128 output channels 2S Z and 5S Y are removed to serve as reference outputs. The remaining 33 acceleration channels are included
 129 in the sensor network. For the JIS, displacement data obtained from double integration of the accelerations are also included in
 130 the output vector. This means that there are $n_d=66$ and $n_d=33$ total outputs for the JIS and DKF, respectively.

131 A finite element (FE) model of the bridge is created in the software ABAQUS; see Fig. 4. This model provides the structural
 132 mass and stiffness matrices (\mathbf{M}_s and \mathbf{K}_s). A panel model of the pontoons is created in DNV HydroD WADAM [25], a software
 133 capable of modelling fluid-structure interaction based on linearized potential theory. The hydrodynamic matrices $\mathbf{M}(\omega)$, $\mathbf{C}(\omega)$
 134 and \mathbf{K}_h are exported from this program. The system model is assembled in MATLAB, where system matrices from the FE
 135 and hydrodynamic submodels are joined. More details on how floating structures can be modelled in an FE framework are
 136 provided in [24]. The floating bridge model is updated in the following way: the model is tuned by adjusting mass and stiffness
 137 parameters, such as elastic moduli, densities and spring constants of the support bearings; see [26] for details. The updating
 138 objective is to match the natural frequencies and mode shapes of the system in Eq. 1 (i.e. the "full" wet system) to modal
 139 parameters from a system identification. Note that these modes are complex since the damping in this system is very high due
 140 to the contribution from $\mathbf{C}(\omega)$, and also non-proportional. After the model is updated, the modes from Eq. 8 are constructed,
 141 which are the ones included in the state-space model. These modes are real-valued since proportional damping is assumed for
 142 the linear system in Eq. 5. Because steel structures are commonly lightly damped, the damping ratio $\xi_j = 0.5\%$ is assigned to

Mode	f_j [Hz]	Type	Mode	f_j [Hz]	Type	Mode	f_j [Hz]	Type
m1	0.098	H	m10	0.340	V/H/T	m19	0.825	H/T
m2	0.130	V	m11	0.343	V/H/T	m20	1.03	H/T
m3	0.135	V	m12	0.354	H/T	m21	1.14	H/T
m4	0.155	V	m13	0.396	V	m22	1.24	H/T
m5	0.177	H/T	m14	0.474	H/T	m23	1.32	V
m6	0.198	V	m15	0.490	H/T	m24	1.44	V
m7	0.223	H/T	m16	0.573	H/T	m25	1.57	V
m8	0.264	V	m17	0.615	H/T	m26	1.75	V
m9	0.296	H/T	m18	0.637	H/T	m27	1.90	V/A

Table 1: Modes of the system in Eq. 8. H=horizontal bending, V=vertical bending, T=torsion, A=axial.

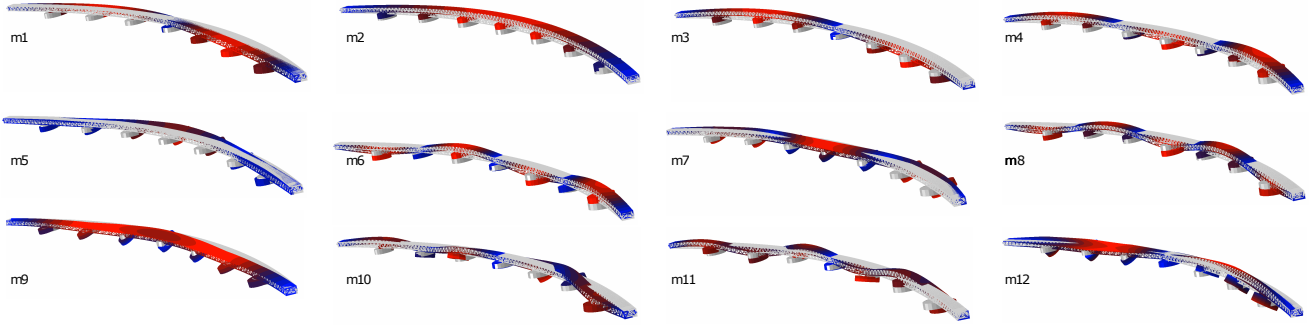


Figure 5: Twelve of the mode shapes from the system model used for the input and state estimation.

143 all of the vibration modes in the linear model. OMA of the bridge shows that the structural damping is in the order of 0.5-1%,
144 with a variation of 20-50% [27].

145 Model validation is important since inverse problems can be sensitive to model errors. For the present case, the (real) modes
146 in the state-space model cannot be directly compared to (complex) modes from a system identification, as the latter ones also
147 include the contribution from the frequency dependent mass and damping. In the model updating the average frequency error
148 is 2.5% and generally a good representation of the mode shapes is acquired. We therefore think the model errors are reasonable
149 low, given the complexity of the structure in this case study.

150 Since the wave loading is the main source of excitation, the response is dominated by frequency content below 2 Hz. To
151 reconstruct the observed dynamic behaviour, it is therefore decided to include the lowermost $n_m = 27$ modes in the reduced-
152 order model. The natural frequencies and mode types are listed in Table 1; a selection of twelve shapes are shown in Fig. 5. All
153 the modes are global and thus influence the output. The majority of the modes can be classified as either pure vertical bending
154 or, due to the curvature of the bridge, a combination of horizontal bending and torsion.

155 3.3. Unknown excitation forces and system invertibility

156 Next, the locations of the unknown excitation forces are defined. Wave forces on pontoon bridges are commonly modelled
157 in an FE format as three concentrated forces and three concentrated moments acting in the centre of each pontoon; see Fig. 6

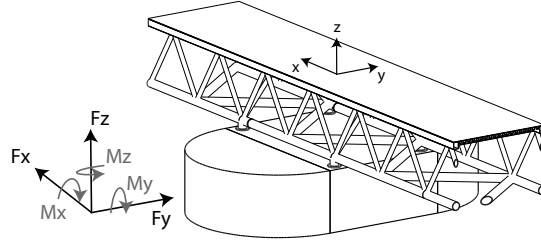


Figure 6: Sketch of the modelling of the wave forces on the pontoons.

158 for an illustration. In feasibility studies of force identification on the Bergsøysund Bridge, numerical simulations showed that
 159 not all six components have a significant influence on the output [28]. The forces F_y and F_z and the moment M_x govern the
 160 dynamics of the bridge; thus, the components F_x , M_y and M_z are neglected ($n_p = 7 \times 3 = 21$).

161 The use of the algorithms in Section 3.1 requires fulfilling fundamental conditions for instantaneous system inversion. The
 162 conditions are related to the system model and to the sensor network [29]. The requirements that are listed below are necessary
 163 to fulfil but do not guarantee a successful estimation; they only reflect the estimation feasibility from an algorithmic perspective.

- 164 – System observability is necessary for state estimation and is fulfilled if and only if the matrix $[\mathbf{S}_d \Phi \quad \mathbf{S}_d \Phi]$ has no zero
 165 columns. Here, the observability condition is fulfilled since all the modes in the model are captured by at least one
 166 acceleration or displacement output.
- 167 – Direct invertibility ensures that the system can be inverted without time delay, translating to the condition $\text{rank}(\mathbf{J}) = n_p$,
 168 where \mathbf{J} is the direct transmission matrix in Eq. 14. This condition implies that the number of acceleration outputs must
 169 be greater than or equal to the number of unknown forces ($n_p \leq n_{d,a}$) and that the number of forces cannot exceed the
 170 number of modes in the model ($n_p \leq n_m$). Here, it is readily found that $\text{rank}(\mathbf{J}) = 21 = n_p$.
- 171 – Stability concerns whether a unique system inversion is possible and is governed by the system transmission zeros $\lambda_j \in \mathbb{C}$,
 172 which are solutions of the following equation:

$$\begin{bmatrix} \mathbf{A} - \lambda_j \mathbf{I} & \mathbf{B} \\ \mathbf{G} & \mathbf{J} \end{bmatrix} \begin{bmatrix} \mathbf{x}_0 \\ \mathbf{p}_0 \end{bmatrix} = \begin{bmatrix} \mathbf{0} \\ \mathbf{0} \end{bmatrix} \quad (22)$$

173 The presence of transmission zeros means that a unique system inversion is impossible since the force $\mathbf{p}_k = \mathbf{p}_0 \lambda_j^k$ ($k =$
 174 $0, 1, \dots, N$) will not be distinguishable from the output. Here, the system model used for the JIS contains no transmission
 175 zeros, whereas the zero $\lambda_j = 1$ occurs for the system model used for the DKF since now only acceleration data are
 176 included in the output vector. The latter is the case of so-called marginal stability.

177 We conclude that response estimation is feasible, while keeping in mind the many practical aspects are not covered by the
 178 checked conditions (e.g. FE model errors, errors on the locations of the forces or coloured noise).

Recording no.	1	2	3
Recording start time	Nov. 08 2015 19:56	Nov. 16 2015 05:37	Dec. 30 2015 03:20
Duration [min]	30	30	30
Mean wind velocity [m/s]	12.08, 10.37, 8.23	10.84, 9.11, 8.66	15.64, 14.54, 13.84
SWH [m]	0.61, 0.54, 0.43	0.35, 0.31, 0.26	0.92, 0.81, 0.73

Table 2: Statistics reported for 10 minute intervals for each of the recordings.

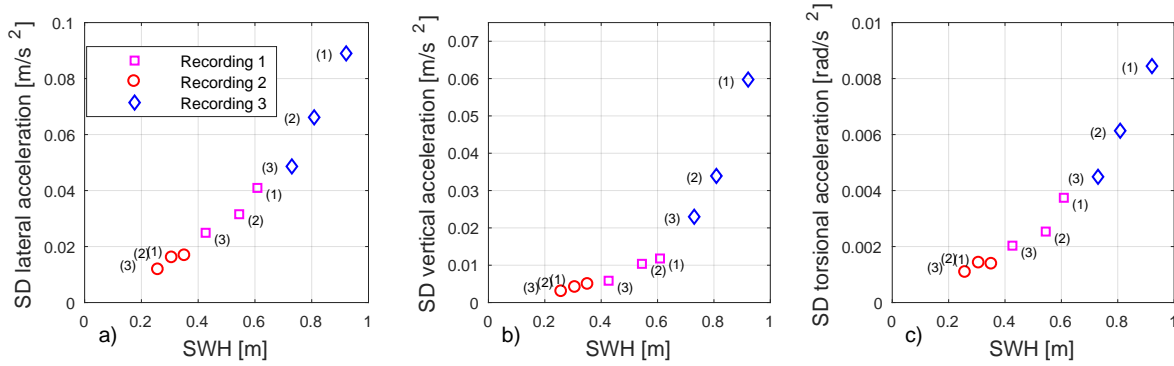


Figure 7: Significant wave height versus standard deviation of the acceleration in the lateral direction (a), vertical direction (b) and torsion (c), measured at the middle pontoon. The number in parentheses denotes the respective 10-minute interval of each recording.

4. Estimation of the dynamic response

4.1. Data recordings

Three recordings are chosen as data sets for the case study. The recordings, which are listed in Table 2, are selected on the basis of representing a variety of the ambient load conditions occurring at the site. The statistics in Table 2 are reported for 10 minute intervals because the fjord areas have shorter periods of stationarity than, for instance, off-shore open waters. Here, the listed significant wave heights (SWHs) are approximated as four times the standard deviation of the wave elevation measured by the wave radars [30], and the mean wind velocities are reported for the midmost anemometer. The response excitation levels are also shown in Fig. 7. The responses should follow a linear trend with the SWH. The observed response is follows a slightly steeper than linear trend since the peak period tend to shift down with an increase in SWH. The power spectral densities (PSDs) in Fig. 8 show that the wave energy has its highest concentration in the range 0.3-0.5 Hz. For more information on the metocean characteristics at Bergsøysundet, see [23].

All acceleration data are originally sampled at 200 Hz but are filtered below 0.07 Hz and above 1.95 Hz using a Chebyshev type II filter and resampled to $F_s = 20$ Hz ($\Delta t = 0.05$ s). The displacement data are generated by a double numerical integration of the accelerations and subsequent frequency-domain filtering (Chebyshev type II), removing spurious content below 0.07 Hz. The first and last 60 s of the time series are removed to disregard transient filtering content.

4.2. Tuning of the error covariance matrices

Next, the choice of covariance parameters for tuning of the filters is discussed. For most practical cases, the errors (or noise) are not known a priori. However, a number of techniques or rules of thumb for establishing the covariances can be found in the

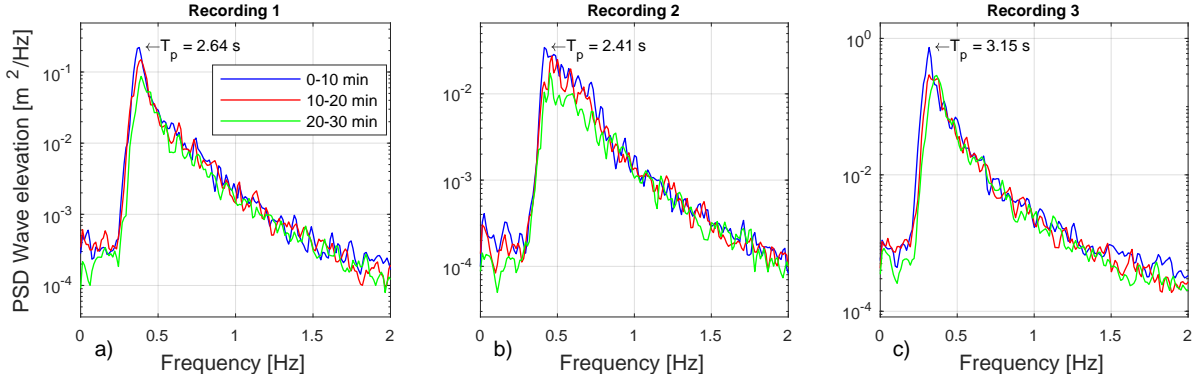


Figure 8: PSD of the wave elevation for the three recordings taken from the midmost wave radar.

197 literature. Strategies for filtering out stochastic excitation (e.g. wind) at unknown locations have been proposed [10]. In other
 198 cases, the covariances can be manually tuned to a level where the results (either state or input estimates) are deemed realistic.
 199 Here, the following measurement error covariance is assigned:

$$\mathbf{R} = \alpha_R \text{diag}(\sigma_{y,1}^2, \sigma_{y,2}^2, \dots, \sigma_{y,n_d}^2) \quad (23)$$

200 where the scale factor $\alpha_R = 0.01$ is used. Note that the description of the noise processes in Eq. 16-17 only covers white
 201 noise. In practice, the addition of errors on the FE model and the presence of excitation forces at other locations than the wave
 202 forces inherently results in coloured noise processes, which the filtering algorithms are not designed to account for. As is the
 203 case for many practical problems with an uncertain and complicated error picture, the chosen covariance in Eq. 23 can only
 204 be argued to be a "best practice" solution without a true basis from optimal theory. The following covariance matrix for the
 205 process noise is assigned:

$$\mathbf{Q} = \mathbf{I} \quad (24)$$

206 In comparison, the modal responses are expected to be in the order of $1 - 10^2$ based on (forward) numerical simulations of
 207 the bridge to wave actions. Note that the presence of errors on the model also implies that in reality $\mathbf{S} \neq 0$ [31]. However, since
 208 these errors (and their inherent correlations) are unknown, \mathbf{S} is set equal to zero in this application.

209 For the DKF, the force covariance is also an important control variable. The following simple force regularization model is
 210 adopted:

$$\mathbf{Q}_P = \gamma_P \begin{bmatrix} \mathbf{I}_{14 \times 14} & \mathbf{0} \\ \mathbf{0} & 10^2 \cdot \mathbf{I}_{7 \times 7} \end{bmatrix} \quad (25)$$

211 where γ_P is a tuning variable, and a larger step value is assigned to the seven moments, which typically are an order of
 212 magnitude larger than the forces. L-curve-type approaches are often the go-to option for determining an appropriate amount of
 213 regularization (see, e.g. [32] for a mathematical description or [5, 12, 33] for practical use). The technique is, however, based on
 214 cases where the measurement errors are dominant [33]. A "derived L-curve" approach is nevertheless adopted here as a measure
 215 to determine the influence of the force covariance. Using real data, the DKF algorithm is run repeatedly with several values for

216 γ_P ; Figs. 9a, 10a and 11a show the influence of the force covariance on the fitting of the data using the mean innovation error
 217 norm ($\frac{1}{N+1} \sum_{k=0}^N \|\mathbf{y}_k - \mathbf{G}\hat{\mathbf{x}}_k - \mathbf{J}\hat{\mathbf{p}}_k\|_2^2$) as a control metric. Since model errors cannot be neglected for the present case, the curves
 218 do not resemble the characteristic L-shape (Figs. 9b, 10b and 11b). However, a minimum is observed in the innovation error for
 219 a given γ_P value. In the following, the values for γ_P are respectively chosen as $10^{7.75}$, $10^{7.0}$, and $10^{8.0}$ for the three recordings.
 220 Compared with the SWHs in the three recordings, the order of difference between the γ_P values is deemed realistic. Note that
 221 the filtering algorithms also allow time-varying noise covariance matrices. This can be relevant for cases with non-stationary
 222 excitation, where the optimal amount of regularization can vary throughout the time series. Although variations in the ambient
 223 conditions occur, constant covariance matrices are used for each recording in this study.

224 4.3. Response prediction

225 The accelerations are now reconstructed at the reference sensor DOFs (2S Z and 5S Y) using the algorithms in Section 3.1
 226 together with Eq. 21. The time series results are shown in Figs. 12, 14 and 16. Table 3 lists the normalized root mean square
 227 error (NRMSE) for the estimated accelerations, which is calculated using Eq. 26 for each of the two reference channels. From
 228 Figs. 9c, 10c and 11c, it is observed that the DKF is indeed sensitive to the force regularization but that the innovation error
 229 minimum generally also corresponds a low NRMSE for reference 5S Y but not for 2S Z. A trend for all the recordings is that
 230 2S Z experiences significantly higher errors than 5S Y. The effect of the errors can be observed in the PSDs in Figs. 13, 15 and
 231 17. Here, it is clear that the bridge dynamics is indeed highly complex, as a great amount of modes are observed to contribute
 232 to the total response. In general, the errors are the largest above 1 Hz, where the acceleration estimates appear to "blow up".
 233 The JIS is slightly more prone to this ill-conditioning than the DKF.

234 The largest errors are observed for the second recording. This result may be explained by the low SWH compared to the
 235 wind velocity (cf. Table 2). If the wave forces are no longer the dominant source of excitation, this translates to a larger model
 236 and measurement error. In recordings 1 and 3, the errors are smaller.

237 Traffic loading is a disturbance not accounted for in the description of the forces. We however find it unlikely that this is the
 238 cause of errors in the high frequency range since the errors generally occur through the entire time series. It is also expected
 239 that very few cars pass the bridge at night, when recording 2 and 3 was taken.

Acceleration output reference	Recording 1		Recording 2		Recording 3	
	JIS	DKF	JIS	DKF	JIS	DKF
2S Z	0.703	0.662	1.095	0.820	0.596	0.562
5S Y	0.222	0.252	0.452	0.455	0.200	0.251

Table 3: NRMSE of the estimated accelerations of the two reference DOFs.

$$\text{NRMSE} = \sqrt{\frac{1}{N+1} \sum_{k=0}^N \frac{(y_k - \hat{y}_k)^2}{\sigma_y^2}} \quad (26)$$

240 As discussed in Section 3.2, the model used is calibrated by FE model updating. This calibrated model has a 3-7% difference
 241 in natural frequencies compared to an uncalibrated one. It is also interesting to see the how an uncalibrated model performs,
 242 since model updating is not always feasible in all experimental studies. We have therefore also run the analysis with the

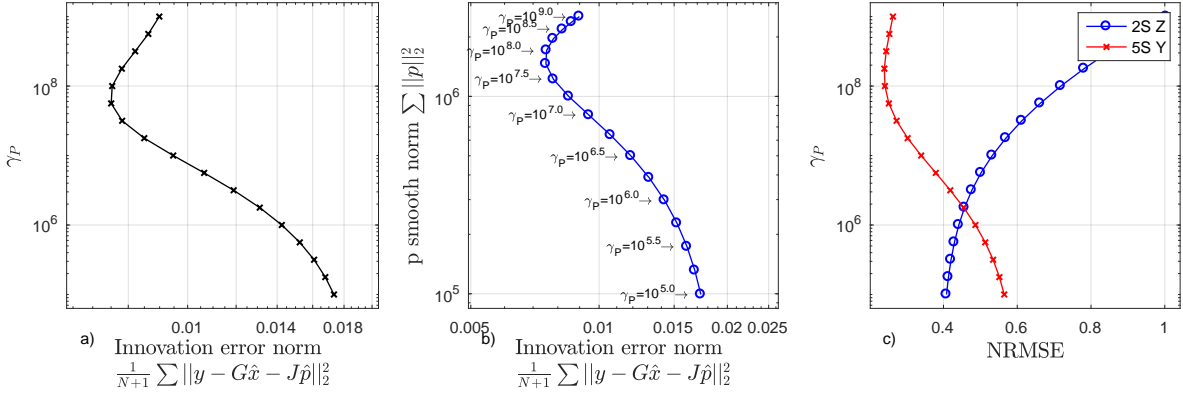


Figure 9: Influence of force covariance in the DKF for recording 1.

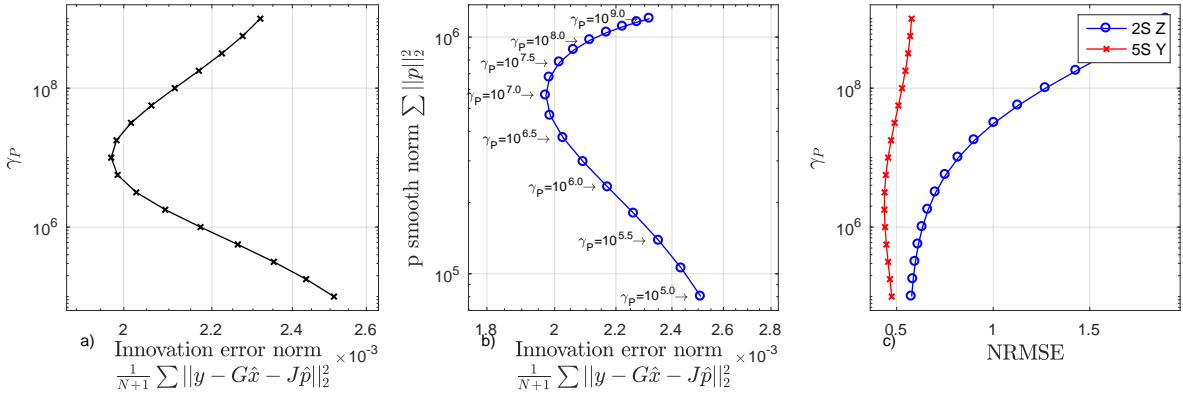


Figure 10: Influence of force covariance in the DKF for recording 2.

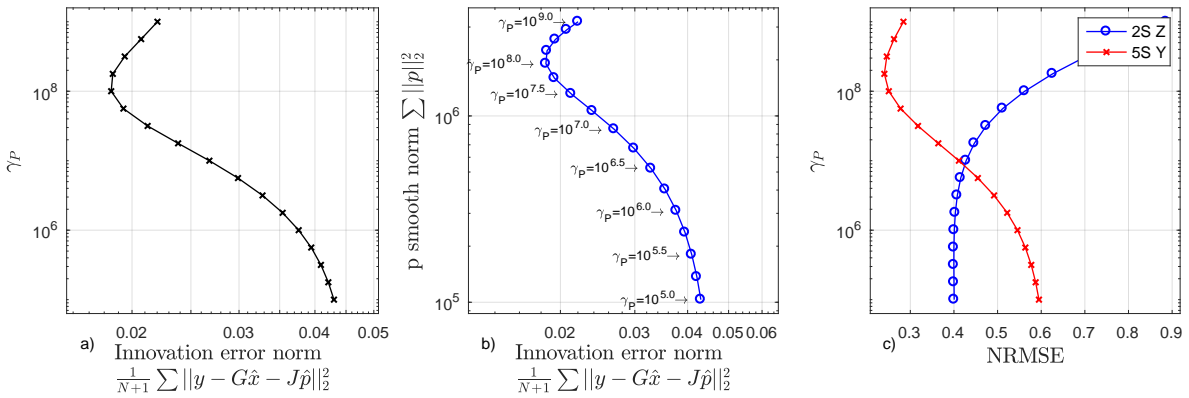


Figure 11: Influence of force covariance in the DKF for recording 3.

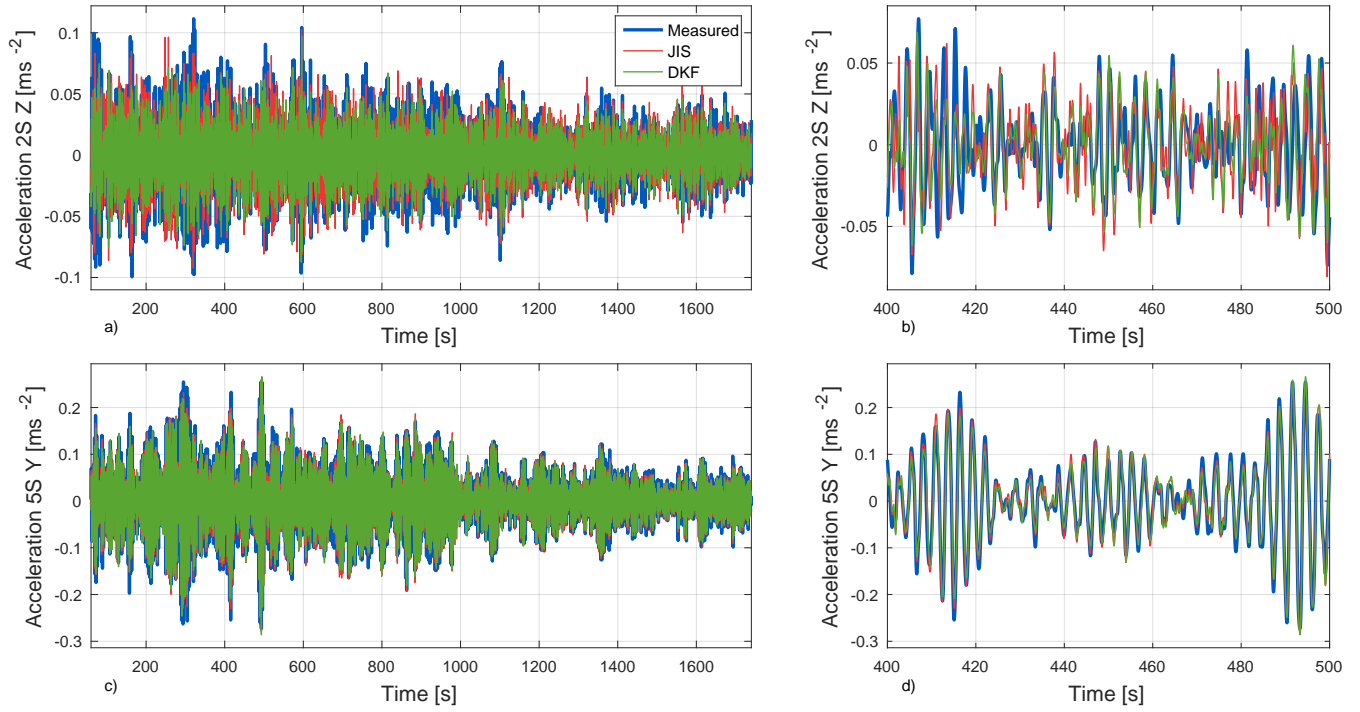


Figure 12: Estimated acceleration response in recording 1 compared to reference measurements.

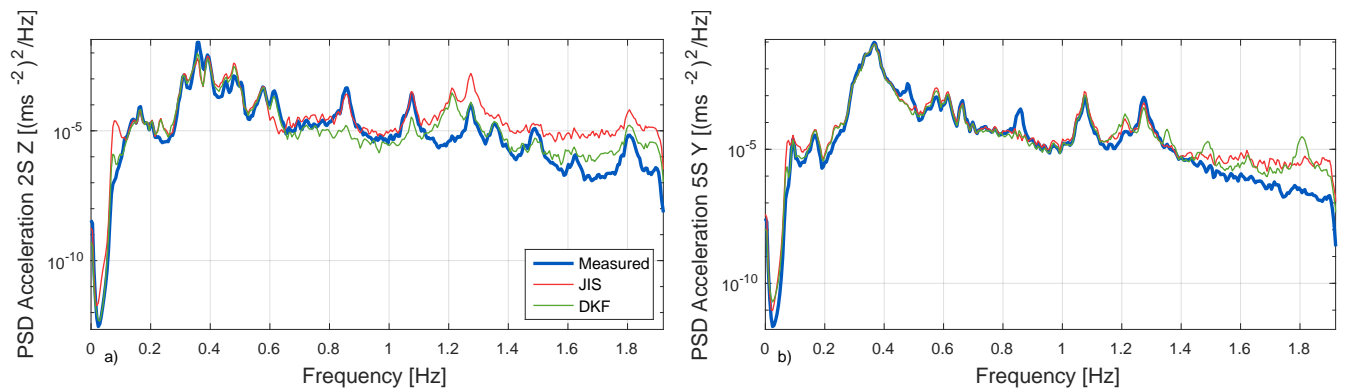


Figure 13: PSDs of the estimated acceleration response in recording 1 compared to the measured reference.

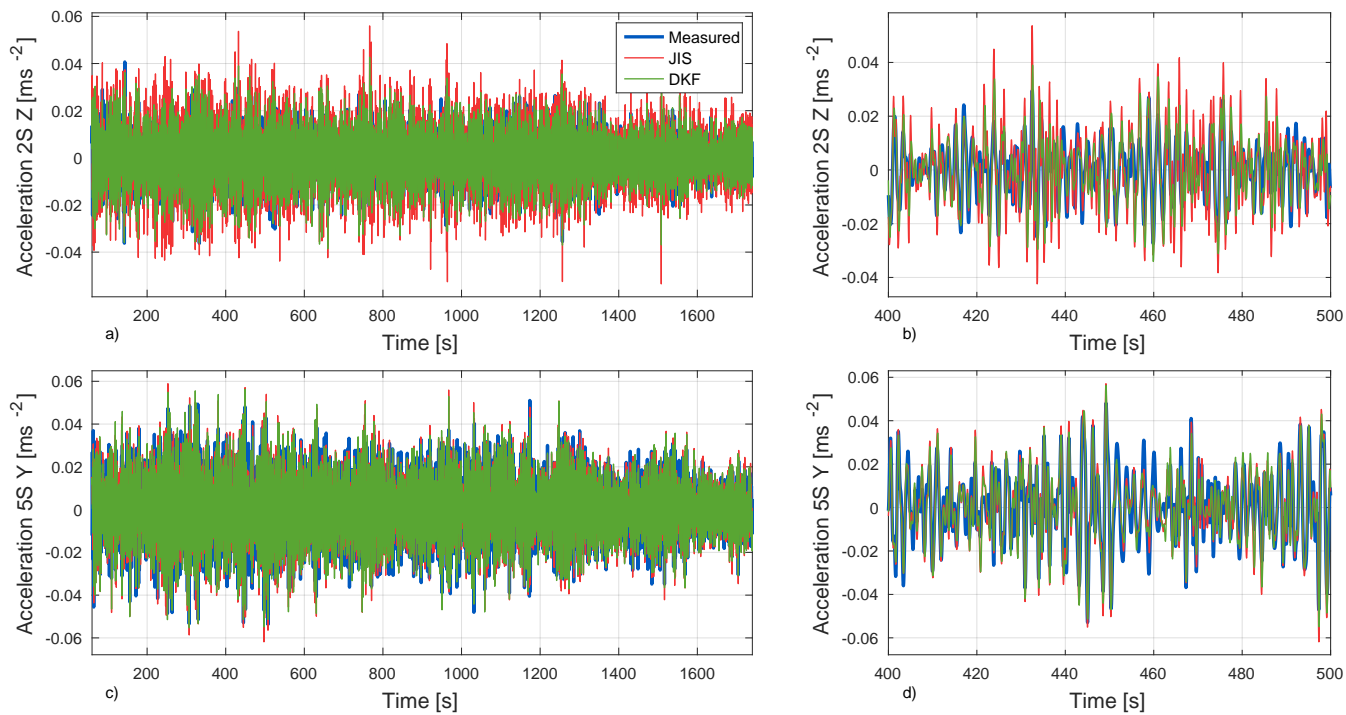


Figure 14: Estimated acceleration response in recording 2 compared to reference measurements.

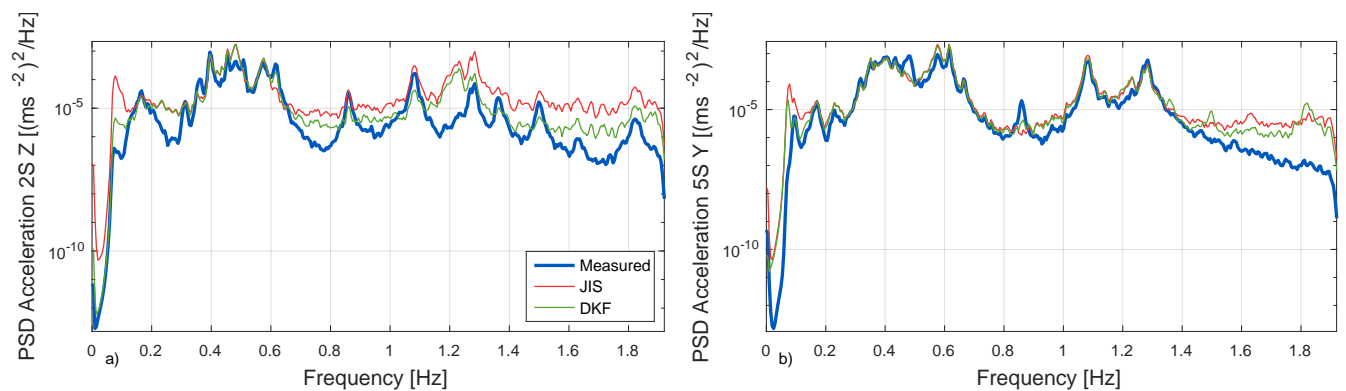


Figure 15: PSDs of the estimated acceleration response in recording 2 compared to the measured reference.

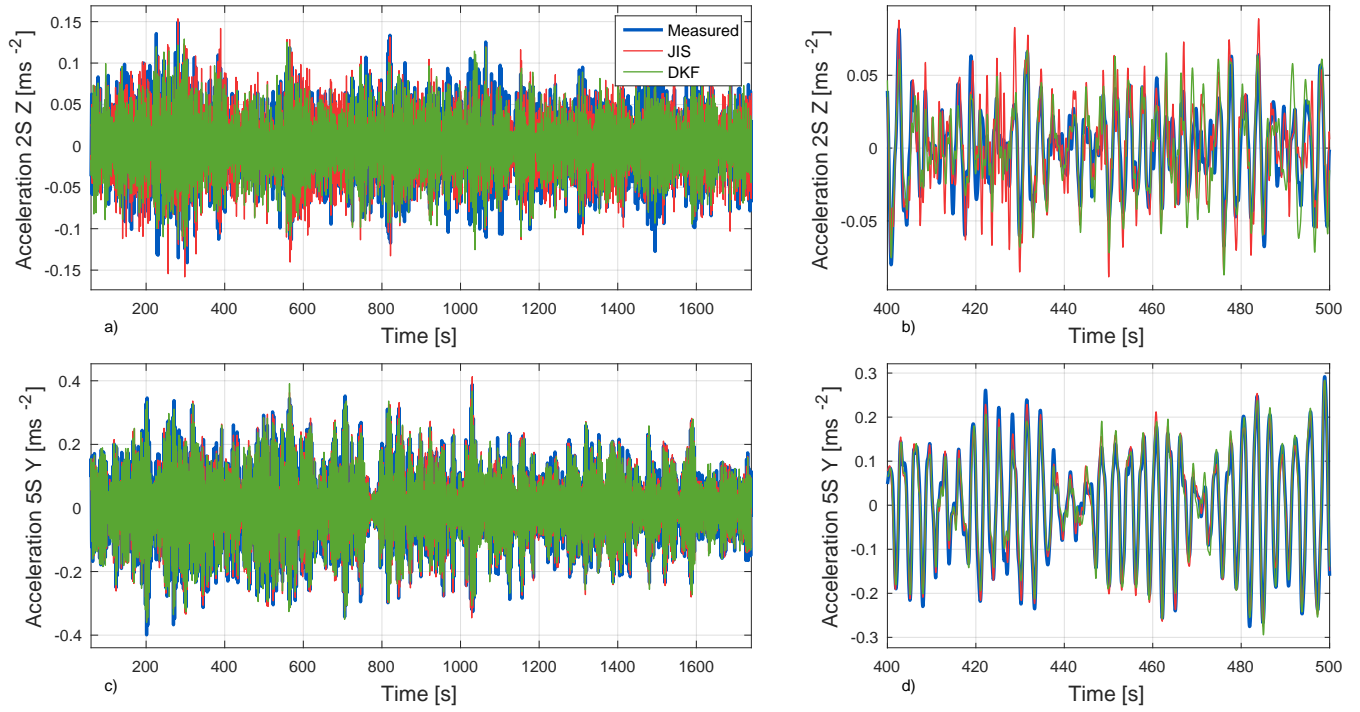


Figure 16: Estimated acceleration response in recording 3 compared to reference measurements.

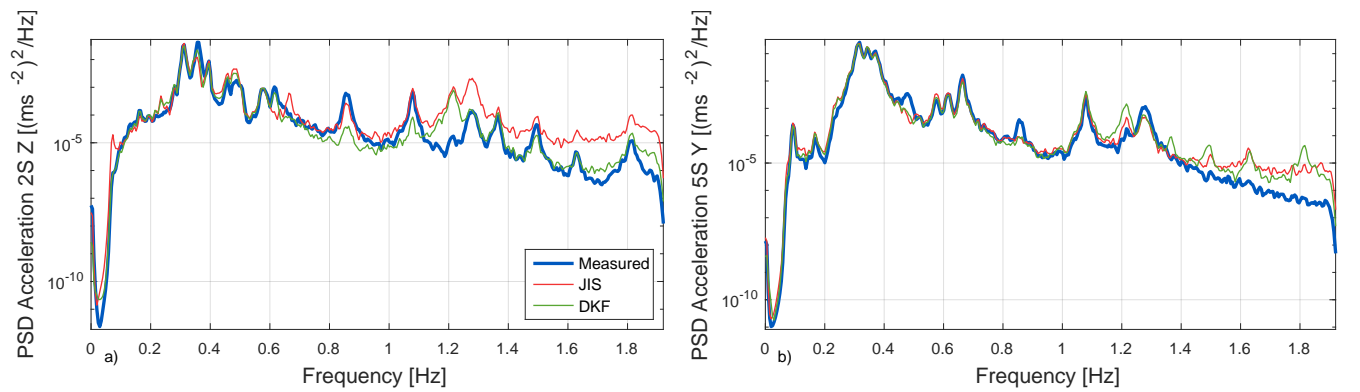


Figure 17: PSDs of the estimated acceleration response in recording 3 compared to the measured reference.

243 uncalibrated model as a check. This results in an increase of 1-5% for the errors in Table 3 , meaning that the updating is not
244 always imperative for accurate results.

245 Since displacement data is included in the output for the JIS, the covariance and gain matrices in the filter equations converge
246 to a steady state. When these converged matrices are used for the entire time series the computational time is highly reduced,
247 especially for large systems. The computations are performed in MATLAB on a laptop with a quad-core 2.1 GHz processor/16
248 GB RAM. Here, each recording (30 minutes or 36000 time steps) is processed in approximately 1 s for the JIS. This means that
249 for the present case the JIS can in theory be implemented in online processing of measurement data, where it is necessary that
250 the calculation time for each time step is smaller than the sample time step. Even so, a conflict here is that the displacement
251 data is obtained from integration of accelerations, which is an offline procedure. Due to the aforementioned transmission zero
252 for the DKF ($\lambda=1$), a steady state is not reached in this algorithm. Therefore, each recording requires approximately 10 s
253 to process. In addition, if L-curves or other regularization plots are sought, multiple (offline) runs must be performed.

254 4.4. Estimation of displacement response

255 The displacement response of the bridge is highly important because it dictates, e.g. the dynamic cross-sectional forces and
256 strain cycles. Although the bridge was designed to resist fatigue, steel components at the support have been replaced due to
257 fatigue damage. Fatigue is known to be a challenging failure mode for marine structures due to the uncertainties related to the
258 load environment and the difficulties of applying laboratory data to in-service structures.

259 Using Eq. 20, the displacements are now estimated at the middle of the bridge where the GNSS sensor is located. As the
260 displacement data are included in the output vector for the JIS, no further (frequency domain) filtering of the state estimates is
261 required. Although the system inversion is marginally stable for the DKF (cf. Section 3.3), no spurious low-frequency instabilities
262 ("drift") in the state estimate are encountered.

263 Recording 2 is discarded in this section since the excitation is too small for the GNSS sensor to provide meaningful data.
264 Figs. 18 and 20 present comparisons of the displacement estimates to the independent GNSS measurements for recordings
265 1 and 3. The GNSS signal contents below 0.07 Hz and above 1.95 Hz are also filtered out to isolate the modal dynamics.
266 However, from the PSD plots in Figs. 19 and 21, it is clear that the GNSS data contain a substantial amount of noise throughout
267 the frequency range of interest. For both considered recordings, the largest peak in the PSD is observed at 0.3-0.4 Hz, which
268 corresponds well to the peak wave periods registered by the wave radars ($T_p = 2.64$ s and 3.15 s, cf. Fig. 8). For frequencies
269 higher than 0.4 Hz, only a few peaks can be distinguished in the GNSS data (ca. 0.50 Hz and 0.85 Hz), and the response energy
270 level is barely sufficient to penetrate the noise floor. In addition, satellite-based position data typically have less accuracy for
271 the vertical (Z) component, which is why the lateral (Y) measurements generally have the highest signal-to-noise ratio (SNR).
272 No quantification of the filter performance is presented here because the GNSS noise corrupts any meaningful error metric. In
273 the time domain, a good correspondence between the GNSS measurements and displacement estimates can be observed for
274 the lateral direction (Figs. 18d and 20d), but the SNR is generally too small in the axial and vertical components for the same
275 conclusion to be drawn. However, both the JIS and DKF are able to capture the dynamics of the dominant frequency band at
276 0.3-0.4 Hz. Although both filter estimates are similar below 0.4 Hz, for higher frequencies, discrepancies are found. This result
277 can be traced to the higher-order modal dynamics contained within the state estimates, which is generally more sensitive than
278 the lower modes to the chosen covariance matrices. Therefore, the discrepancy should not be given too much emphasis. The

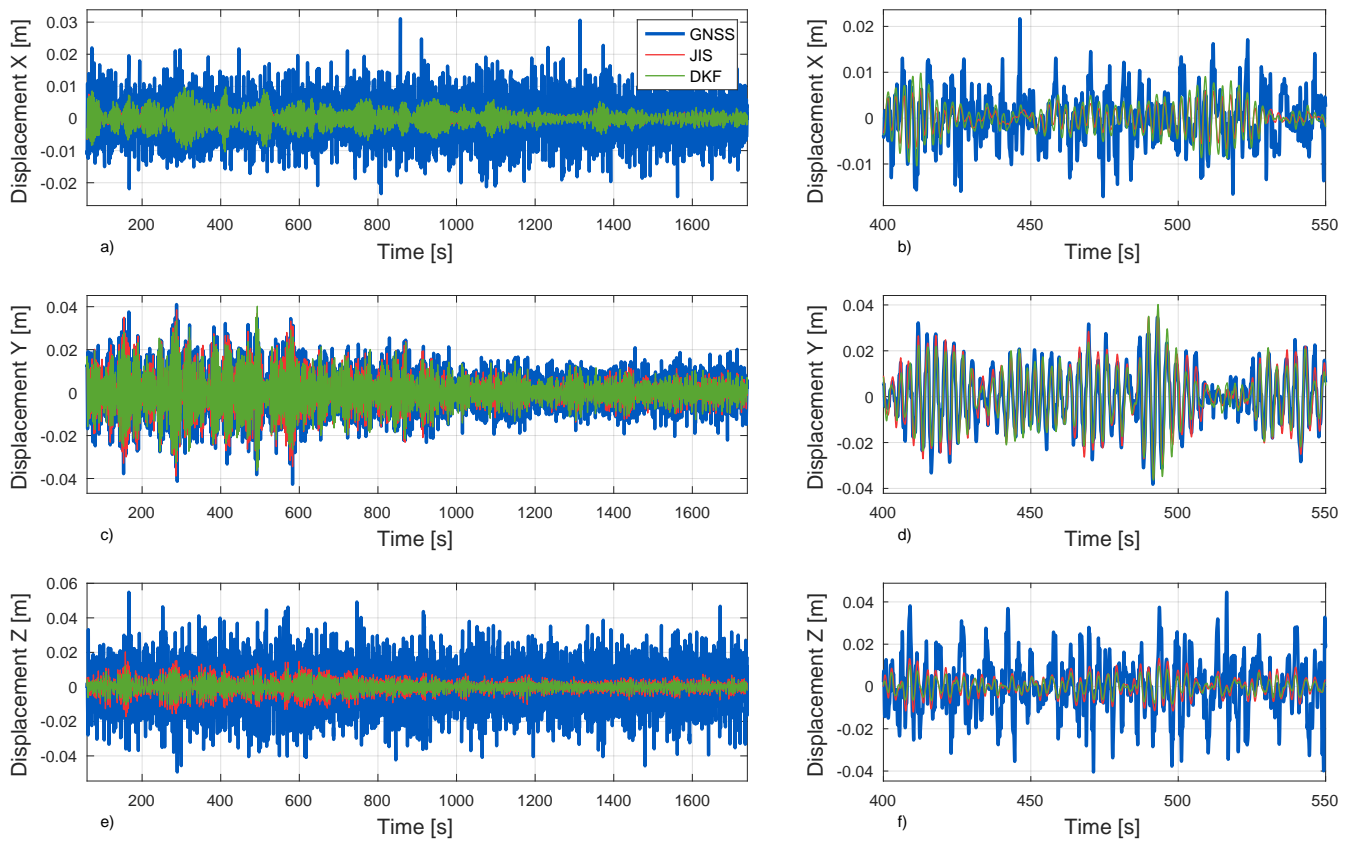


Figure 18: Estimated displacement history in recording 1 compared to GNSS measurements.

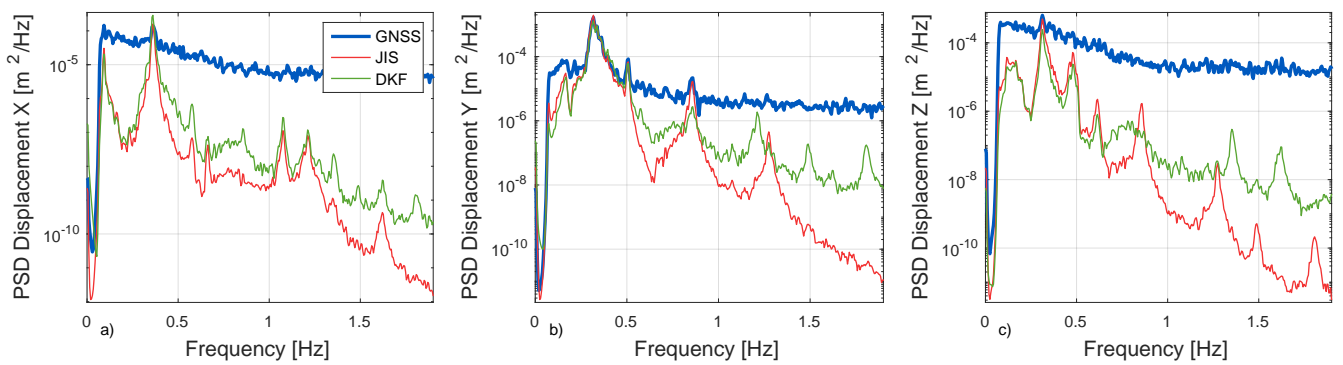


Figure 19: PSDs of the estimated displacements in recording 1 compared to GNSS measurements.

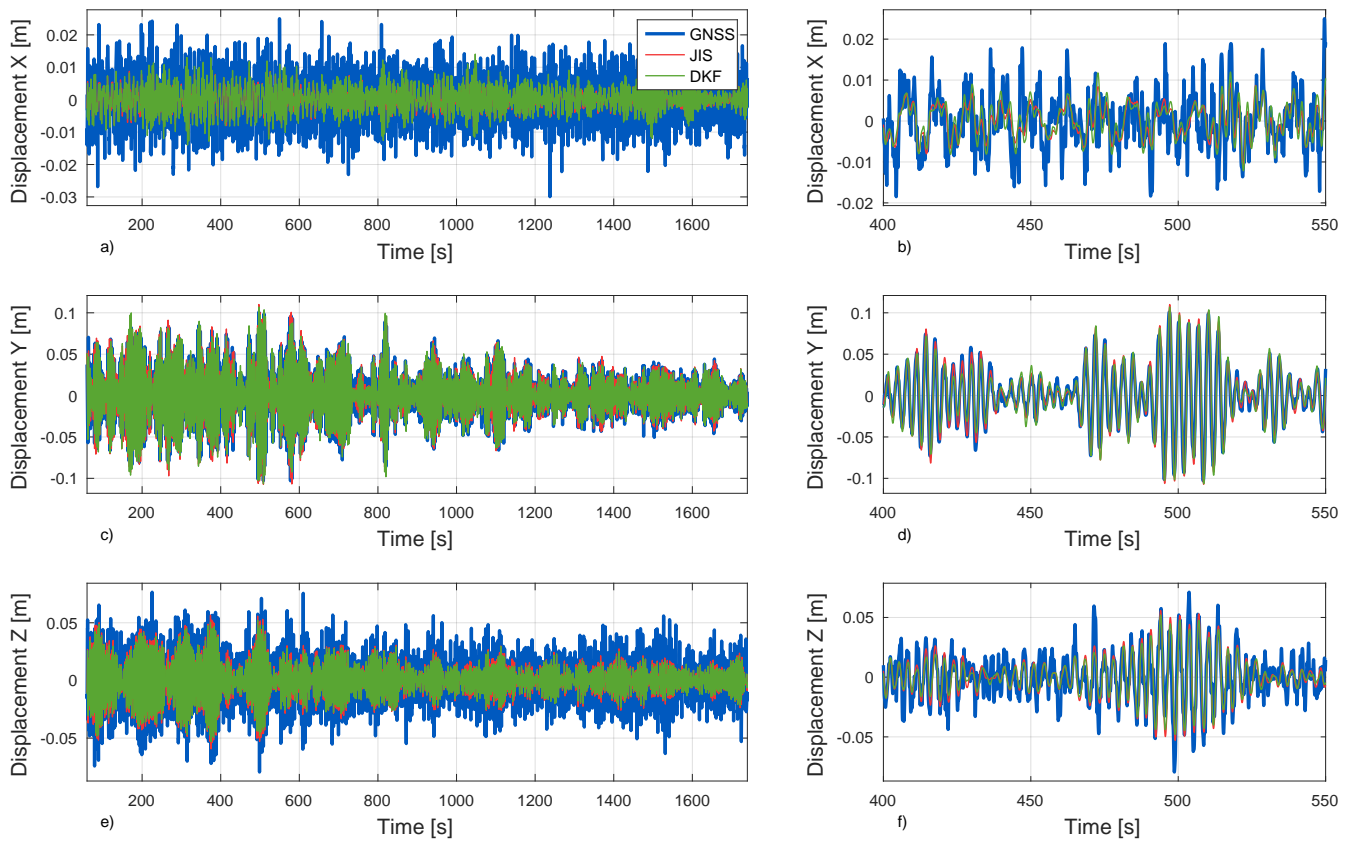


Figure 20: Estimated displacement history in recording 3 compared to GNSS measurements.

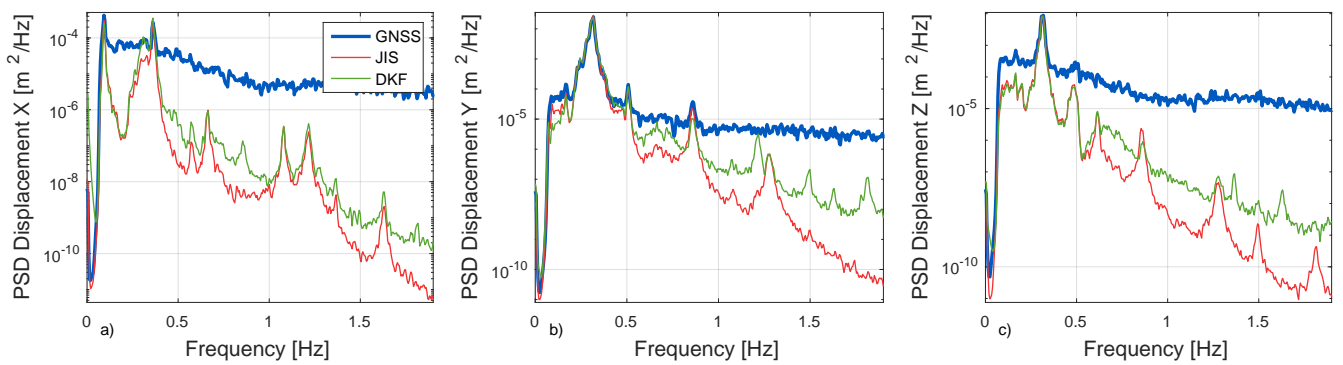


Figure 21: PSDs of the estimated displacements in recording 3 compared to GNSS measurements.

279 response magnitude in the high-frequency range is however very small compared to the overall peak magnitude; thus, the two
280 filters yield very similar temporal results.

281 The results presented here generally agree with previous assessments of the performance of the GNSS sensor [23], where
282 it was concluded that the satellite-based data have a significant noise floor. Large amplitude excitation is therefore required
283 for a high SNR. This can be observed in the first ten minutes of recording 1 or throughout recording 3, for example. In these
284 time periods, the best match of the peaks and valleys is acquired. Note that these levels of response, i.e. amplitudes above
285 10 cm, are among the largest observed over the course of one year of monitoring [23]. Certainly, the results indicate that
286 the implementation of dynamic GNSS measurements as a validation tool can be suitable for more flexible structures, such as
287 long-span suspension bridges.

288 5. Conclusion

289 This paper presented a case study of full-field response estimation on the Bergsøysund Bridge, which is a long-span pontoon
290 bridge that is excited mainly by wave forces. The dynamic response was estimated using two well-established filter algorithms
291 for state and input estimation, which utilize a reduced-order system model and measured acceleration data. Three different data
292 recordings with varying ambient conditions were used in the analysis. It was found that the accelerations can be reconstructed
293 at unmeasured locations with moderate errors. The errors generally increase when the wave forces on the pontoons are not the
294 dominant source of excitation. In the validation of the displacement estimate, it was shown that for large amplitude excitation,
295 the filter estimates agree well with the motion measured by an independent GNSS sensor. For small excitation levels, the sensor
296 noise in the GNSS inhibits proper validation.

297 Overall, the results confirm that the presented methodology is applicable to large-scale structures with a highly complex
298 dynamic behaviour. However, the studies indicate that the use of inverse methods on these structures still has many practical
299 challenges. In particular, model errors and stochastic excitation at unknown locations remain as adverse sources of error for the
300 estimated response.

301 Acknowledgements

302 This work was financially supported by the Norwegian Public Roads Administration.

303 Appendix A

304 *Joint input-state estimation:*

Initial quantities:

$$\text{State estimate: } \hat{\mathbf{x}}_{0|-1} \tag{A.1}$$

$$\text{State error covariance: } \mathbf{P}_{0|-1} \tag{A.2}$$

Input estimation:

$$\tilde{\mathbf{R}}_k = \mathbf{G}\mathbf{P}_{k|k-1}\mathbf{G}^T + \mathbf{R} \quad (\text{A.3})$$

$$\mathbf{M}_k = (\mathbf{J}^T\tilde{\mathbf{R}}_k^{-1}\mathbf{J})^{-1}\mathbf{J}^T\tilde{\mathbf{R}}_k^{-1} \quad (\text{A.4})$$

$$\hat{\mathbf{p}}_{k|k} = \mathbf{M}_k(\mathbf{y}_k - \mathbf{G}\hat{\mathbf{x}}_{k|k-1}) \quad (\text{A.4})$$

$$\mathbf{P}_{\mathbf{p}[k|k]} = (\mathbf{J}^T\tilde{\mathbf{R}}_k^{-1}\mathbf{J})^{-1} \quad (\text{A.5})$$

Measurement update:

$$\mathbf{L}_k = \mathbf{P}_{k|k-1}\mathbf{G}^T\tilde{\mathbf{R}}_k^{-1} \quad (\text{A.6})$$

$$\hat{\mathbf{x}}_{k|k} = \hat{\mathbf{x}}_{k|k-1} + \mathbf{L}_k(\mathbf{y}_k - \mathbf{G}\hat{\mathbf{x}}_{k|k-1} - \mathbf{J}\hat{\mathbf{p}}_{k|k}) \quad (\text{A.7})$$

$$\mathbf{P}_{k|k} = \mathbf{P}_{k|k-1} - \mathbf{L}_k(\tilde{\mathbf{R}}_k - \mathbf{J}\mathbf{P}_{\mathbf{p}[k|k]}\mathbf{J}^T)\mathbf{L}_k^T \quad (\text{A.8})$$

$$\mathbf{P}_{\mathbf{xp}[k|k]} = \mathbf{P}_{\mathbf{px}[k|k]}^T = -\mathbf{L}_k\mathbf{J}\mathbf{P}_{\mathbf{p}[k|k]} \quad (\text{A.9})$$

Time update:

$$\hat{\mathbf{x}}_{k+1|k} = \mathbf{A}\hat{\mathbf{x}}_{k|k} + \mathbf{B}\hat{\mathbf{p}}_{k|k} \quad (\text{A.10})$$

$$\mathbf{N}_k = \mathbf{A}\mathbf{L}_k(\mathbf{I} - \mathbf{J}\mathbf{M}_k) + \mathbf{B}\mathbf{M}_k \quad (\text{A.11})$$

$$\mathbf{P}_{k+1|k} = \begin{bmatrix} \mathbf{A} & \mathbf{B} \end{bmatrix} \begin{bmatrix} \mathbf{P}_{k|k} & \mathbf{P}_{\mathbf{xp}[k|k]} \\ \mathbf{P}_{\mathbf{px}[k|k]} & \mathbf{P}_{\mathbf{p}[k|k]} \end{bmatrix} \begin{bmatrix} \mathbf{A}^T \\ \mathbf{B}^T \end{bmatrix} + \mathbf{Q} - \mathbf{N}_k\mathbf{S}^T - \mathbf{S}\mathbf{N}_k^T \quad (\text{A.12})$$

305

Dual Kalman filter:

Initial quantities:

$$\text{Force estimate: } \hat{\mathbf{p}}_0 \quad (\text{A.13})$$

$$\text{Force error covariance: } \mathbf{P}_0^{\mathbf{p}} \quad (\text{A.14})$$

$$\text{State estimate: } \hat{\mathbf{x}}_0 \quad (\text{A.15})$$

$$\text{State error covariance: } \mathbf{P}_0 \quad (\text{A.16})$$

Prediction of the input:

$$\mathbf{p}_k^- = \mathbf{p}_{k-1} \quad (\text{A.17})$$

$$\mathbf{P}_k^{p^-} = \mathbf{P}_{k-1}^p + \mathbf{Q}_P \quad (\text{A.18})$$

Kalman gain and filter estimate for the input:

$$\mathbf{G}_k^p = \mathbf{P}_k^{p^-}\mathbf{J}^T(\mathbf{J}\mathbf{P}_k^{p^-}\mathbf{J}^T + \mathbf{R})^{-1} \quad (\text{A.19})$$

$$\hat{\mathbf{p}}_k = \mathbf{p}_k^- + \mathbf{G}_k^p(\mathbf{y}_k - \mathbf{G}\hat{\mathbf{x}}_{k-1} - \mathbf{J}\mathbf{p}_k^-) \quad (\text{A.20})$$

$$\mathbf{P}_k^p = \mathbf{P}_k^{p^-} - \mathbf{G}_k^p\mathbf{J}\mathbf{P}_k^{p^-} \quad (\text{A.21})$$

Prediction of the state:

$$\mathbf{x}_k^- = \mathbf{A}\hat{\mathbf{x}}_{k-1} + \mathbf{B}\hat{\mathbf{p}}_k \quad (\text{A.22})$$

$$\mathbf{P}_k^- = \mathbf{A}\mathbf{P}_{k-1}\mathbf{A}^T + \mathbf{Q} \quad (\text{A.23})$$

Kalman gain and filter estimate for the state:

$$\mathbf{G}_k^x = \mathbf{P}_k^- \mathbf{G}^T (\mathbf{G}\mathbf{P}_k^- \mathbf{G}^T + \mathbf{R})^{-1} \quad (\text{A.24})$$

$$\hat{\mathbf{x}}_k = \mathbf{x}_k^- + \mathbf{G}_k^x (\mathbf{y}_k - \mathbf{G}\mathbf{x}_k^- - \mathbf{J}\hat{\mathbf{p}}_k) \quad (\text{A.25})$$

$$\mathbf{P}_k = \mathbf{P}_k^- - \mathbf{G}_k^x \mathbf{G}\mathbf{P}_k^- \quad (\text{A.26})$$

306 References

- 307 [1] A. Iliopoulos, R. Shirzadeh, W. Weijtjens, P. Guillaume, D. V. Hemelrijck, C. Devriendt, A modal decomposition and
 308 expansion approach for prediction of dynamic responses on a monopile offshore wind turbine using a limited number of
 309 vibration sensors, *Mechanical Systems and Signal Processing* 68-69 (2016) 84–104.
- 310 [2] A. Iliopoulos, W. Weijtjens, D. Van Hemelrijck, C. Devriendt, Fatigue assessment of offshore wind turbines on monopile
 311 foundations using multi-band modal expansion, *Wind Energy* 20 (8) (2017) 1463–1479, ISSN 1099-1824, we.2104.
- 312 [3] A. Skafté, U. T. Tygesen, R. Brincker, Expansion of mode shapes and responses on the offshore platform Valdemar, in:
 313 *Dynamics of Civil Structures, Volume 4*, Springer, 35–41, 2014.
- 314 [4] A. Skafté, J. Kristoffersen, J. Vestermark, U. T. Tygesen, R. Brincker, Experimental study of strain prediction on wave
 315 induced structures using modal decomposition and quasi static Ritz vectors, *Engineering Structures* 136 (2017) 261–276.
- 316 [5] E. Lourens, E. Reynders, G. De Roeck, G. Degrande, G. Lombaert, An augmented Kalman filter for force identification
 317 in structural dynamics, *Mechanical Systems and Signal Processing* 27 (2012) 446–460.
- 318 [6] J.-S. Hwang, S.-G. Lee, P. Ji-hoon, Y. Eun-Jong, Force identification from structural responses using Kalman filter, in:
 319 *Materials Forum*, vol. 33, 2009.
- 320 [7] C. K. Ma, J. M. Chang, D. C. Lin, Input forces estimation of beam structures by an inverse method, *Journal of Sound and*
 321 *Vibration* 259 (2) (2003) 387–407.
- 322 [8] S. Pan, H. Su, H. Wang, J. Chu, The study of joint input and state estimation with Kalman filtering, *Transactions of the*
 323 *Institute of Measurement and Control* 33 (8) (2011) 901–918.
- 324 [9] E. Lourens, C. Papadimitriou, S. Gillijns, E. Reynders, G. De Roeck, G. Lombaert, Joint input-response estimation for
 325 structural systems based on reduced-order models and vibration data from a limited number of sensors, *Mechanical*
 326 *Systems and Signal Processing* 29 (2012) 310–327.
- 327 [10] K. Maes, A. Smyth, G. De Roeck, G. Lombaert, Joint input-state estimation in structural dynamics, *Mechanical Systems*
 328 *and Signal Processing* 70–71 (2016) 445–466.

- 329 [11] K. Maes, K. Van Nimmen, E. Lourens, A. Rezayat, P. Guillaume, G. De Roeck, G. Lombaert, Verification of joint input-
330 state estimation for force identification by means of in situ measurements on a footbridge, *Mechanical Systems and Signal*
331 *Processing* 75 (2016) 245–260.
- 332 [12] S. E. Azam, E. Chatzi, C. Papadimitriou, A dual Kalman filter approach for state estimation via output-only acceleration
333 measurements, *Mechanical Systems and Signal Processing* 60 (2015) 866–886.
- 334 [13] S. E. Azam, E. Chatzi, C. Papadimitriou, A. Smyth, Experimental Validation of the Dual Kalman Filter for Online and
335 Real-Time State and Input Estimation, in: *Model Validation and Uncertainty Quantification, Volume 3*, Springer, 1–13,
336 2015.
- 337 [14] S. E. Azam, E. Chatzi, C. Papadimitriou, A. Smyth, Experimental validation of the Kalman-type filters for online and
338 real-time state and input estimation, *Journal of Vibration and Control* 23 (15) (2015) 2494–2519.
- 339 [15] K. Maes, S. Gillijns, G. Lombaert, A smoothing algorithm for joint input-state estimation in structural dynamics, *Me-*
340 *chanical Systems and Signal Processing* 98 (2018) 292–309.
- 341 [16] K. Maes, A. Iliopoulos, W. Weijtjens, C. Devriendt, G. Lombaert, Dynamic strain estimation for fatigue assessment
342 of an offshore monopile wind turbine using filtering and modal expansion algorithms, *Mechanical Systems and Signal*
343 *Processing* 76-77 (2016) 592–611.
- 344 [17] T. S. Nord, E. Lourens, O. Øiseth, A. Metrikine, Model-based force and state estimation in experimental ice-induced
345 vibrations by means of Kalman filtering, *Cold Regions Science and Technology* 111 (2015) 13–26.
- 346 [18] T. S. Nord, O. Øiseth, E. Lourens, Ice force identification on the Nordstrømsgrund lighthouse, *Computers & Structures*
347 169 (2016) 24–39.
- 348 [19] L. Zhi, Q. Li, M. Fang, Identification of Wind Loads and Estimation of Structural Responses of Super-Tall Buildings by
349 an Inverse Method, *Computer-Aided Civil and Infrastructure Engineering* 31 (12) (2016) 966–982.
- 350 [20] Y. Niu, C.-P. Fritzen, H. Jung, I. Bueth, Y.-Q. Ni, Y.-W. Wang, Online simultaneous reconstruction of wind load and
351 structural responses: theory and application to Canton tower, *Computer-Aided Civil and Infrastructure Engineering* 30 (8)
352 (2015) 666–681.
- 353 [21] J. Ko, Y. Ni, Technology developments in structural health monitoring of large-scale bridges, *Engineering structures*
354 27 (12) (2005) 1715–1725.
- 355 [22] Ø. W. Petersen, O. Øiseth, T. S. Nord, E. Lourens, Response estimation for a floating bridge using acceleration output
356 only, in: *Proceedings of the 27th Conference on Noise and Vibration Engineering (ISMA 2016)*, 19-21 September 2016,
357 Leuven, Belgium, 613–625, 2016.
- 358 [23] K. A. Kvåle, O. Øiseth, Structural monitoring of an end-supported pontoon bridge, *Marine Structures* 52 (2017) 188–207.
- 359 [24] K. A. Kvåle, R. Sigbjörnsson, O. Øiseth, Modelling the stochastic dynamic behaviour of a pontoon bridge: A case study,
360 *Computers & Structures* 165 (2016) 123–135.

- 361 [25] DNV Software, HydroD WADAM 9.1 User Manual, 2014.
- 362 [26] Ø. Petersen, O. Øiseth, Sensitivity-based finite element model updating of a pontoon bridge, *Engineering Structures* 150
363 (2017) 573–584.
- 364 [27] K. A. Kvåle, O. Øiseth, A. Rønnquist, Operational modal analysis of an end-supported pontoon bridge, *Engineering*
365 *Structures* 148 (2017) 410–423.
- 366 [28] Ø. W. Petersen, O. Øiseth, T. S. Nord, E. Lourens, Model-Based Estimation of Hydrodynamic Forces on the Bergsoysund
367 Bridge, in: *Proceedings of the 34th IMAC, A Conference and Exposition on Structural Dynamics, Dynamics of Civil*
368 *Structures, Volume 2*, Springer, 217–228, 2016.
- 369 [29] K. Maes, E. Lourens, K. Van Nimmen, E. Reynders, G. De Roeck, G. Lombaert, Design of sensor networks for instantane-
370 ous inversion of modally reduced order models in structural dynamics, *Mechanical Systems and Signal Processing* 52
371 (2014) 628–644.
- 372 [30] L. H. Holthuijsen, *Waves in oceanic and coastal waters*, Cambridge University Press, 2010.
- 373 [31] E. Lourens, D. Fallais, On the use of equivalent forces for structural health monitoring based on joint input-state estimation
374 algorithms, *Procedia Engineering* 199 (Supplement C) (2017) 2140 – 2145, ISSN 1877-7058, X International Conference
375 on Structural Dynamics, EUROLYN 2017.
- 376 [32] P. C. Hansen, *The L-curve and its use in the numerical treatment of inverse problems*, IMM, Department of Mathematical
377 Modelling, Technical University of Denmark, 1999.
- 378 [33] K. Tatsis, E. Lourens, A comparison of two Kalman-type filters for robust extrapolation of offshore wind turbine support
379 structure response, in: *Life-Cycle of Engineering Systems: Emphasis on Sustainable Civil Infrastructure: Proceedings*
380 *of the Fifth International Symposium on Life-Cycle Civil Engineering (IALCCE 2016)*, 16-19 October 2016, Delft, The
381 Netherlands, CRC Press, 59, 2016.